**Supporting Information template**

*Geophysical Research Letters*

Supporting Information for

# Pre-explosive conduit conditions during the 2010 eruption of Merapi volcano (Java, Indonesia)

Mélissa J. DRIGNON [1], Tonin BECHON [2,3], Laurent ARBARET [2,3], Alain BURGISSER [4*], Jean-Christophe KOMOROWSKI [5], Caroline MARTEL [2,3], Hayden MILLER [6], Radit YAPUTRA [7]

[1] College of Earth, Ocean and Atmospheric Sciences, Oregon State University, Corvallis, OR, USA.

[2] Université d'Orléans, ISTO, F-45071 Orléans, France.

[3] CNRS, ISTO, F-45071 Orléans, France.

[4] Université Savoie Mont Blanc, CNRS - INSU, ISTerre, F-73376 Le Bourget du Lac, France.

[5] Institut de Physique du Globe de Paris, Sorbonne Paris Cité, Université Paris Diderot, Paris, France.

[6] Division of Geological and Planetary Sciences, Caltech, Pasadena, CA, USA.

[7] Pusat Vulkanologi dan Mitigasi Bencana Geologi, CVGHM, Yogyjakarta, Indonesia

## Contents of this file

Text S1 to S3
Additional references
Figures S1 to S6
Tables S1 to S5

## Introduction

Text sections S1-S3 contain details on, respectively, sampling, analytical methods, and the physical model used. Figures S1-S2 display additional methodological information, Figs. S3-S4 graphically report data from Table S2. Fig. S5 displays outputs from the depth reconstruction listed in Table S5. Fig. S6 measures uncertainties of the EDS textural analysis. Table S1 contains data reported graphically in Fig. 1, Table S2-S4 report textural information summarized in the main text, and Table S5 contains data reported graphically in Figs. 2-3. Model outputs for the October 26 and November 5 samples are available at:

https://isterre.fr/annuaire/pages-web-du-personnel/alain-burgisser/article/softwares?lang=fr.

**Text S1.**

October 26 (stage 2) pumices were taken from a locality in the Gendol River, where most of the material erupted that day was emplaced, near the village of Kaliadem (7°35.30' S, 110°27.083' E). We sampled a pumice levee sandwiched between two depositional sub-units of the valley-filling October 26 deposits. In-situ carbonized bamboo remains within the deposits, demonstrating that the pumice and ash units are in place and that the pumice levee was formed during the early phases of the event (Fig. S1). We sampled ~100 variably sized pumice clasts and classified them in the field based on macroscopic textural observations. Seven classes were defined: AME10A are low-density pumices with glass fibers without preferential orientation (PO), patchy large vesicles and few round vesicles, AME10B are low-density pumices with broken glass fibers and rare round vesicles, AME10C are low-density pumices with glass fibers with PO and patchy vesicles, AME10D are low-density pumices with round vesicles, AME10E are dense pumices, AME10F are dense, dark dome clasts, and AME10G are dense pumices with vesicle-rich, glassy areas.

November 5 (stage 6) pumices were taken from two localities. The first one is in the upper Gendol valley near the village of Kaliadem (7°34.834' S, 110°26.850' E). This outcrop is smaller than the one in the lower Gendol valley but also contains evidence that the deposits are in place. A continuous fine ash layer seals the outcrop and we sampled the largest pumices (AME19A) in lobe remnants from the November 5 pyroclastic density current deposits. The second locality is in the lower Gendol valley near the village of Bakalan (7°39.338' S, 110°27.737'E). Sample MER13-01 is composed by pumice found atop of the deposit, above a 0.5 cm fine ash layer that caps the stage 4 deposits. This locality corresponds to point 10 from Komorowski et al. (2013).

**Text S2.**

Textural information was gathered using two methods. In the first method, we acquired at a resolution of 2040×2048 pixels one ×50 image, in which objects 2350-20 µm across can be characterized, and four ×2000 images, in which objects 63-0.5 µm across can be characterized (Giachetti et al., 2010). Image segmentation and object characterization were done using ImageJ 1.48 (imagej.nih.gov/ij/). Phenocrysts, microphenocrysts, vesicles, and oxides >40 µm were segmented in the ×50 image, the remaining surface being attributed to matrix. Here we consider microphenocrysts as being a subset of phenocrysts that are less than 200 µm across

because this limit corresponds to the size above which crystals were manually removed from the powders analyzed for bulk $H_2O$. We choose to set the limit between microphenocryst and microlite to 40 µm across for simplicity. Oxides >40 µm occurring as inclusions in other phenocrysts (generally amphibole) were counted as being part of those phenocrysts. Vesicles and oxides <40 µm were segmented in the ×2000 images while objects >40 µm were ignored because they were already accounted for in the ×50 images. We performed a manual separation of the microlites (mostly plagioclase, Costa et al., 2013) using Adobe Illustrator because the electronic contrast was not sufficient to make an automatic separation (Fig. S2). The manual separation was done on three smaller representative images of about 700×700 pixels that were cropped in the ×2000 images in order to accelerate the manual process by focusing on vesicle-poor parts of the samples. The information from these sub-images was combined to yield one ratio of microlite/glass per ×2000 image. In each sample, object proportions were obtained by assuming equality of area and volume fractions and by combining the objects from the ×50 image with those of the ×2000 images following Giachetti et al. (2010). This yielded up to four series of object proportions, from which a median value and a standard deviation quantifying the natural variability were calculated. Phenocryst and microphenocryst proportions were respectively quantified by a single value because they were only present in the ×50 image. Assuming equality of surface and volume proportions, this procedure yielded bulk objects volumetric proportions of $^0V_{ves}$, $^0V_{ph}$, $^0V_{gl}$, and $^0V_{\mu l}$ (Table S2). In addition, bulk proportions of oxides, $^0V_{ox}$, and microphenocrysts, $^0V_{\mu ph}$, were calculated (Table S3).

In the second method, we used element mapping to accelerate the textural analysis and to better characterize the mineral phases present so as to obtain a more precise estimate of the glass weight fraction in each sample. Element mapping was done by Energy Dispersive X-Ray Spectroscopy (EDS) on 16 of the 37 samples that were crushed according to method B. X-ray maps were obtained at 15 kV with a dwell time of 2 ms per pixel. Each image was filtered by the wavelet "A-trous" filter in ImageJ to decrease the noise level before thresholding. The image processing was done by successive subtractions of Boolean combinations of the elemental maps for two reasons. First, the residual image after all the subtractions quantifies how much of the surface was left out of the analysis. This ensures that no significant mineral phase was ignored. Second, the EDS analysis affects a small volume of the sample. The shallow cusps of bubbles intersecting the upper surface of the polished section often respond to the EDS analysis by indicating the presence of the crystals touching the cusp surface. We use C has a marker of the epoxy filling to make sure that the surface inside such bubbles are properly counted as vesicles and not as crystals or glass. Let $F_{ves}$, $F_{plag}$, $F_{ox}$, $F_{a+cpx}$, $F_{opx}$, $F_{Ca}$, $F_{m+gl}$, and $F_r$ be the final binary images containing respectively vesicles, plagioclase, oxide, amphibole+clinopyroxene, orthopyroxene, Ca-dominant minerals (apatite and Ca-bearing xenoliths), matrix+glass, and residual material. Let $I_i$ be the 9 elemental images per zoom level with i = C, Al, Si, Fe, Mg, Na, Ca, K, and Ti. The series of Boolean manipulations to obtain the final images reads:

$F_{ves} = I_C$ OR NOT($I_{Al}$ OR $I_{Si}$ OR $I_{Fe}$ OR $I_{Mg}$ OR $I_{Na}$ OR $I_{Ca}$ OR $I_K$ OR $I_{Ti}$)

$J_i = I_i - F_{ves}$

$F_{plag} = (J_{Ca}$ AND $J_{Na})$ OR $(J_{Na}$ OR $J_{Al})$

$F_{ox} = (J_{Fe}$ AND $J_{Ti})$

$K_i = J_i - F_{plag} - F_{ox} =$

$F_{a+cpx} = (K_{Ca}$ AND $K_{Fe})$ OR $(K_{Ca}$ AND $K_{Mg})$

$F_{opx} = (K_{Mg} - F_{a+cpx})$ AND $(K_{Fe} - F_{a+cpx})$

$L_i = K_i - F_{a+cpx} - F_{opx}$

$F_{Ca} = L_{Ca>41}$

$F_{m+gl} = L_K$ OR $L_{Fe}$ OR $L_{Mg}$ OR $L_{Ca<41}$ OR $L_{Si}$ OR $L_{Na}$ OR $L_{Al}$

$F_r = 100\% - F_{ves} - F_{plag} - F_{ox} - F_{a+cpx} - F_{opx} - F_{Ca} - F_{m+gl}$ (S1)

where the suffix >41 (<41) means that only objects larger (smaller) than 41 pixel$^2$ are counted in the image so that crystal inclusions are not being subtracted from their host mineral. The sign minus implies image subtraction so that A – B corresponds to A AND NOT B in Boolean notation, and 100% corresponds to a full image area.

We have checked with an optical microscope that the element mapping of the final images represents the main respective mineral phase. The accessory mineral phases not included in our analysis are lumped with the main phases (e.g., xenolithic dolomite). The effect of this approximation is smaller than the spatial variability of the phases as quantified by the multi-scale procedure described below. Residual images (i.e. $F_r$ values) indicate that this procedure classifies >98% of the surface. One step of erosion was done on the $F_{bub}$ images at ×352 and ×2000 to separate (de-coalesce) vesicles and avoid biasing the cut-offs.

Each series of 9 elemental images of 512×384 pixels were taken at 3 magnifications (×35, ×352, and ×2000). The limit is 40 µm between the ×35 and the ×352 images, which matches that between microlite and phenocrysts, and the limit between the ×352 and ×2000 images was set to 10 µm. Method 1 suggests that contiguous glass areas are rarely larger than 10 µm across. So the $F_{m+gl}$ images were assumed to represent glass at ×2000 and matrix at the larger magnifications. An additional limit of 820 µm was set on the ×35 images. It is the maximum size of objects that can be characterized in those images and it corresponds to the size of the large amphibole and pyroxenes ($F_{a+cpx}$ + $F_{opx}$) that were manually removed in the crushing method B. The combination of the three scales follows the procedure described in Giachetti et al. (2010). Between one and four representative images were taken at each magnification. The combinations of these images yielded between 8 and 45 series of object surface proportions, from which a median value and a standard deviation quantifying the natural variability were calculated. Assuming equality of surface and volume proportions, this procedure yielded two series of objects volumetric proportions. The first series takes objects of all sizes into account and it is composed of $^0V_{ves}$, $^0V_{ph}$, $^0V_{gl}$, and $^0V_{µl}$, which correspond to the bulk proportions of vesicle, phenocryst, glass, and microlite, respectively (Table S2). In the second series the amphiboles and pyroxenes ($F_{a+cpx}$ + $F_{opx}$) < 820 µm were removed. The second series is composed of $^1V_{gl}$, $^1V_{ox}$, $^1V_{opx}$, $^1V_{a+cpx}$, and $^1V_{Ca}$, which correspond to the normalized proportions of glass, oxides, orthopyroxenes, amphibole+clinopyroxenes, and Ca-dominant minerals, respectively (Table S4).

The two textural analysis methods were compared on a series of four samples by taking BSE and EDS images on identical locations. The average relative difference on $^0V_{ph}$ is 11%, which is due to a combination of incorrect crystals contouring in the manual procedure and imperfect thresholding in the EDS procedure. This uncertainty is comparable to that caused by natural variability within one sample.

The 21 remaining samples were characterized by optical observations instead of by EDS. The suite of 37 samples that were analyzed with the crushing method B was divided into 12 textural groups by optical microscope observations. At least one sample of each group was analyzed by EDS, and the components proportions of the remaining 21 samples were assumed to be identical to those of the same respective group. This assumption was tested by comparing, for sample pairs belonging to the same textural group, the values $^0V_{ves}$ and the

inverse of the glass weight fraction, which is the quantity that dominates the conversion between bulk and glass $H_2O$ (see Eq. 1 in main text):

$$\frac{\sum_i \rho_i{}^1 V_i}{\rho_{gl}{}^1 V_{gl}} \quad \text{(S2)}$$

The mineral densities were taken from the RRUFF database (rruff.geo.arizona.edu) using the mineral determinations of Costa et al. (2013; amphibole is hastingsite, pyroxene is augite, oxide is magnetite), and the glass density from Conflow (Mastin, 2002) using the glass composition given in Costa et al. (2013). Figure S6 shows that the differences between these two quantities are smaller within a given textural group than the uncertainties linked to the natural spatial variability within each sample.

Using the prefix δ to indicate one standard deviation and omitting the *j* superscripts for clarity, error propagation of Eq. (1) reads:

$$\left(\frac{\delta X_{gl}}{X_{gl}}\right)^2 = \left(\frac{\delta V_{gl}}{V_{gl}}\right)^2 + \frac{\left(\delta X_{bulk}\rho_{equ}\right)^2 + \left(X_{bulk}\delta\rho_{equ}\right)^2 + \left(X_a R \delta V_{a+cpx}\rho_a\right)^2}{\left(X_{bulk}\rho_{equ} - X_a R V_{a+cpx}\rho_a\right)^2} \quad \text{(S3)}$$

where $\rho_{equ} = \sum_i \rho_i V_i$.

**Text S3.**

The recompression model of Burgisser et al. (2010) considers that the magma was stored in the conduit just prior to the explosion as a mixture of melt, crystals, and pre-explosive bubbles caused by degassing during the ascent of the magma from the reservoir. Bubbles are assumed to contain only water, and to be in equilibrium with the melt so that the dissolved water can be related to pressure with the solubility law of Liu et al. (2005) because the glass is close to rhyolitic (Costa et al., 2013). During the explosion, new water bubbles nucleate in response to the sudden decompression linked to the explosion and form two syn-explosive populations: one that is composed of small, isolated bubbles and another that is composed of bubbles that had more time to grow and coalesce. The existing, pre-explosive bubble population also reacts to the explosion by growth and coalescence, which yields a population of large, deformed bubbles. These bubble populations are preserved in the pumices produced by the explosion. We assume that the respective volume proportion of these three populations is given by the textural analysis. A fraction of the gas imprisoned in the bubbles is liberated (outgassed) during the explosion to propel the ejecta. This fraction can only loosely be constrained by independent observations and is thus a free parameter in the model. The thermal and pressure histories of the ejected clasts condition when quench occurs and freezes the textural characteristics of the pumice. Since these histories can rarely be reconstructed (Benage et al., 2014), the model uses an estimate of the maximum, near-instant pressure drop that clasts can sustain before breaking (Mueller et al., 2008) as a proxy for quench pressure. This proxy is modulated by a multiplicative factor that is assumed to lie between 0.5 and 2 with a typical value of 1. The upper limits of the quench pressure factor and the outgassing proportion were chosen so that 1) the maximum total water content of every clast lies below a capping value and 2) that all clasts underwent syn-explosive inflation so as to match textural observations.

**Text S4.**

Taking $CO_2$ into account changes two main aspects of the Burgisser et al. (2010) model. Firstly, $H_2O$ solubility is no longer a simple function of total pressure. The solubility law of Liu et

al. (2005), which is used by the Burgisser et al. (2010) model, is calibrated for a $H_2O$-$CO_2$ mixture and uses partial pressures of $H_2O$ and $CO_2$ instead of total pressure. We thus used the Liu et al. (2005) law to convert melt $H_2O$ content into pre-explosive pressures and added the molar ratio of $CO_2/H_2O$ in the fluid phase as an additional input parameter. Secondly, the molar weight of the fluid phase, $M_T$, is no longer that of pure water but it includes both chemical species:

$$M_T = M_{CO2} + \frac{M_{H2O} - M_{CO2}}{1 + \frac{m_{CO2} M_{CO2}}{(1 - m_{CO2}) M_{H2O}}} \quad \text{(S4)}$$

where $M_{H2O}$, $M_{CO2}$, $m_{H2O}$ and $m_{CO2}$ are respectively the molar weights and molar fractions of $H_2O$ and $CO_2$. This total molar weight is used to calculate the gas density with the ideal gas law. Neglecting in Eq. (S4) the contribution of other chemical species introduces a very small bias as >96 mol% of the fluid phase consists of $H_2O$ and $CO_2$. Both modifications thus involve the addition of the $CO_2/H_2O$ ratio into the Burgisser et al. (2010) model.

Erdmann et al. (2016) suggest that the magma resident in the reservoir feeding the 2010 eruption has a molar ratio of $CO_2/H_2O$ in the fluid phase of 0.4-0.5. They also establish that the pre-eruptive recharge magma was much richer in $H_2O$, with a $CO_2/H_2O$ ratio of ~0.2. The ascent and associated degassing in the conduit has for effect to decrease $CO_2/H_2O$ in the gas phase (e.g., Burgisser et al., 2008). We estimated the maximum amount of $CO_2$ in the fluid phase by taking the highest of these ratios and simulating the decompression of the magma from 250 MPa to the surface using the model D-Compress (Burgisser et al., 2015). Figure S7A shows the respective evolutions of $CO_2/H_2O$ when the ascent occurs under closed- and open-system conditions for initial parameters approaching those at Merapi: rhyolitic melt undergoing isothermal, equilibrium decompression at 950 °C, NNO+1, 4.5 wt% melt $H_2O$, and with an initial $CO_2/H_2O$ of 0.46 (Preece et al., 2014; Erdmann et al., 2016). For simplicity, we selected using Fig. S7A three representative ratios as a function of the pure water pressures originally calculated (Fig. 2). Samples <100 MPa are assumed to have a $CO_2/H_2O$ of 0.1, samples between 100 and 200 MPa have a $CO_2/H_2O$ of 0.2, and samples >200 MPa have a $CO_2/H_2O$ of 0.4.

Figure S7B shows the relative change in pre-explosive pressures as a function of the pure $H_2O$ pressure for the October 26 samples. The effect of $CO_2$ is most marked at high (>200 MPa) pressures, where it would increase the pre-explosive pressures by 150%, which is comparable to measurement uncertainty for those high pressure samples. The $CO_2$ effect is much more moderate (20-40 %) in the other parts of the conduit. Since this is a maximum estimate, we conclude that neglecting $CO_2$ in our analysis means that our pre-explosive pressures are underestimated by an amount at most comparable to measurement uncertainties.

**Additional references**

Benage, M.C., J. Dufek, W. Degruyter, D. Geist, K. Harpp and E. Rader (2014), Tying textures of breadcrust bombs to their transport regime and cooling history, J. Volcanol. Geotherm. Res., 274, 92-107.

Burgisser, A., B. Scaillet, and Harshvardhan (2008), Chemical patterns of erupting silicic magmas and their influence on the amount of degassing during ascent, Journal of Geophysical Research, 113(B12), doi:10.1029/2008JB005680.

Burgisser, A., M. Alletti, and B. Scaillet (2015), Simulating the behavior of volatiles belonging to the C-O-H-S system in silicate melts under magmatic conditions with the software D-Compress, Computers & Geosciences, 79, 1–14.

Liu, Y., Y. Zhang, and H. Behrens (2005), Solubility of $H_2O$ in rhyolitic melts at low pressures and a new empirical model for mixed $H_2O$-$CO_2$ solubility in rhyolitic melts, J. Volcanol. Geotherm. Res., 143, 219-235.

Mastin, L. G. (2002), Insights into volcanic conduit flow from an open-source numerical model, Geochemistry, Geophysics, Geosystems, 3, doi:10.1029/2001GC000192

Mueller, S., B. Scheu, O. Spieler, and D. B. Dingwell (2008), Permeability control on magma fragmentation, Geology, 36, 399–402.

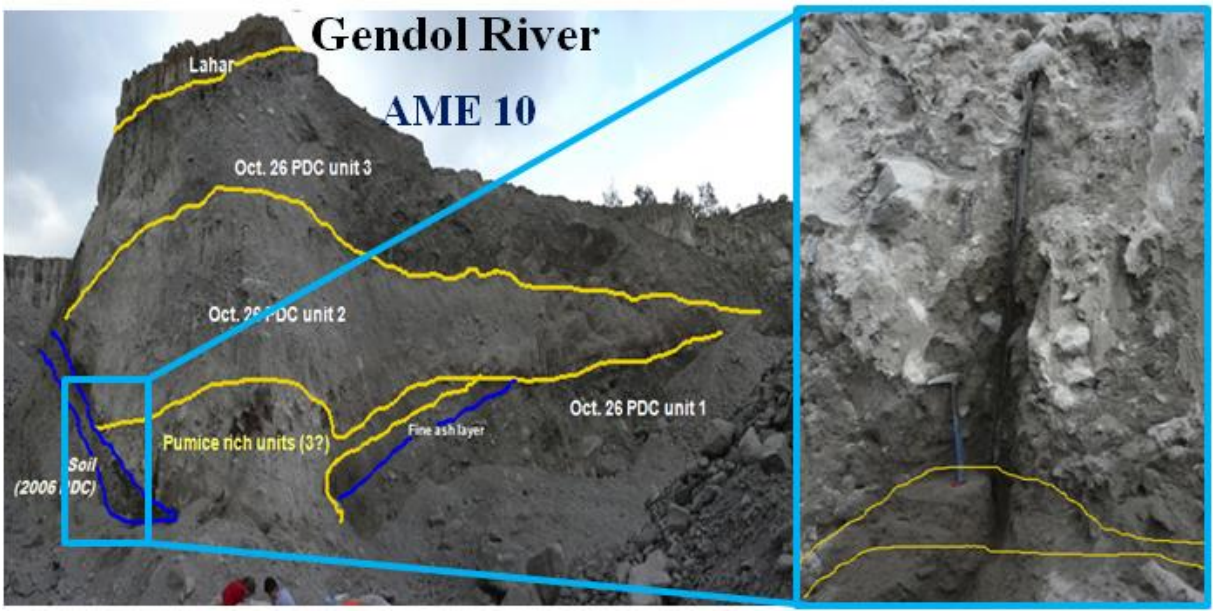


**Figure S1.** Outcrop located within the Gendol River showing the sampled pumice-rich level, which correspond to a flow levee. This location features three depositional units from the pyroclastic density current (PDC) of October 26, 2010. The inset shows charred bamboo that indicates that the pumice levee formed during the early stages of the October 26 event.

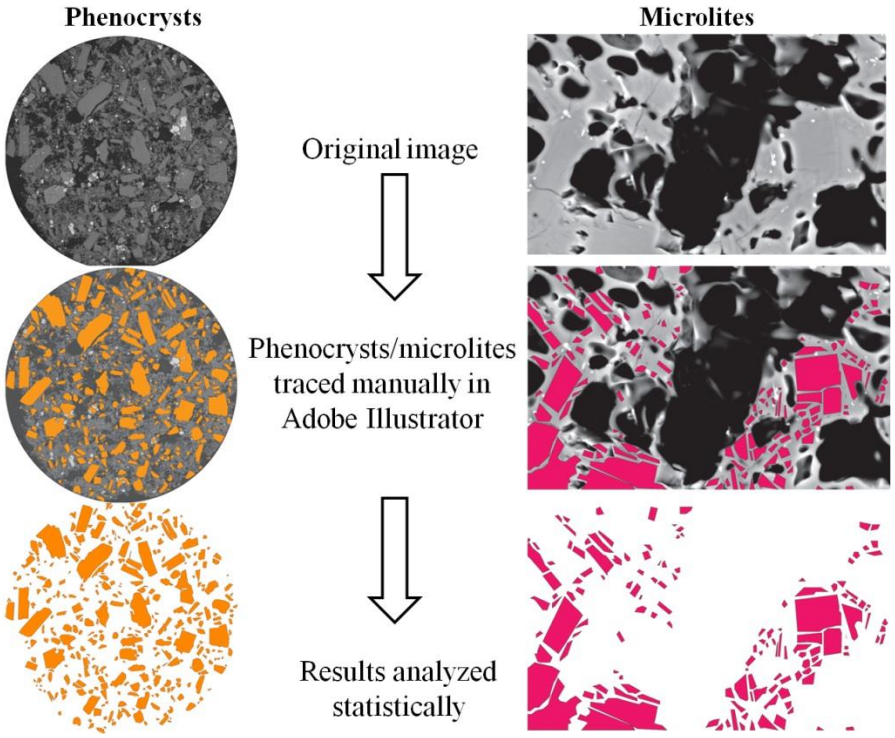


**Figure S2.** Illustration of the textural analysis procedure. SEM images showing phenocrysts (left, x50 images) and interstitial glass with microlites (right, x2000 images). The phenocrysts (orange) and the microlites (pink) have been traced by hand before being segmented and quantified.

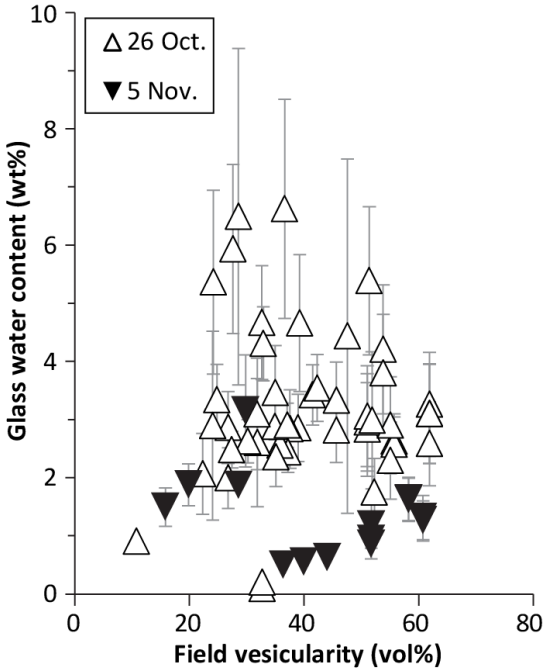


**Figure S3.** Glass water concentration as a function of the field vesicularity.

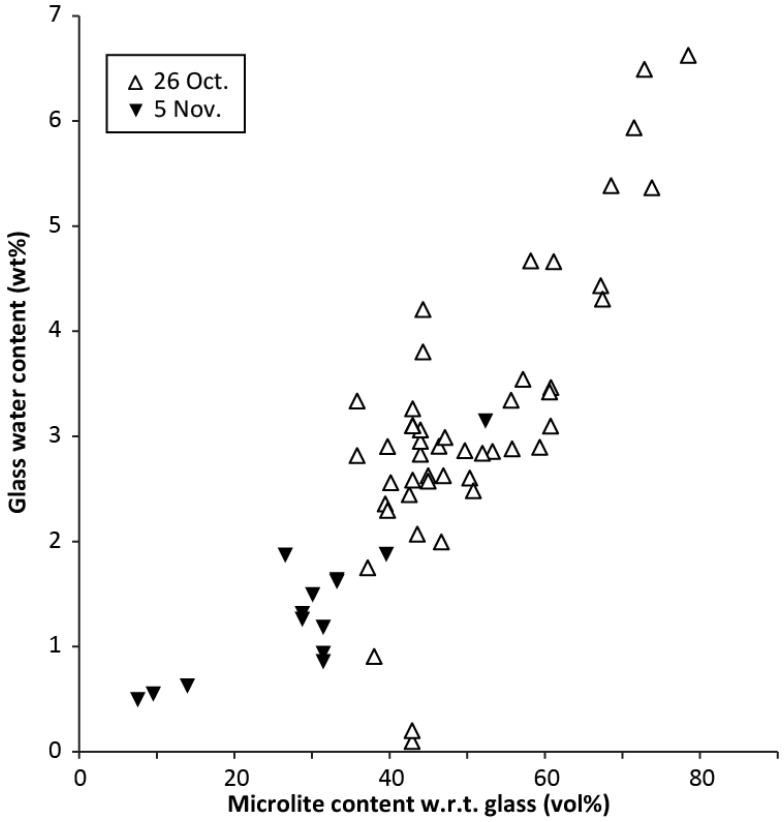


**Figure S4.** Microlite content with respect to (glass plus microlite) as a function of glass water concentration.

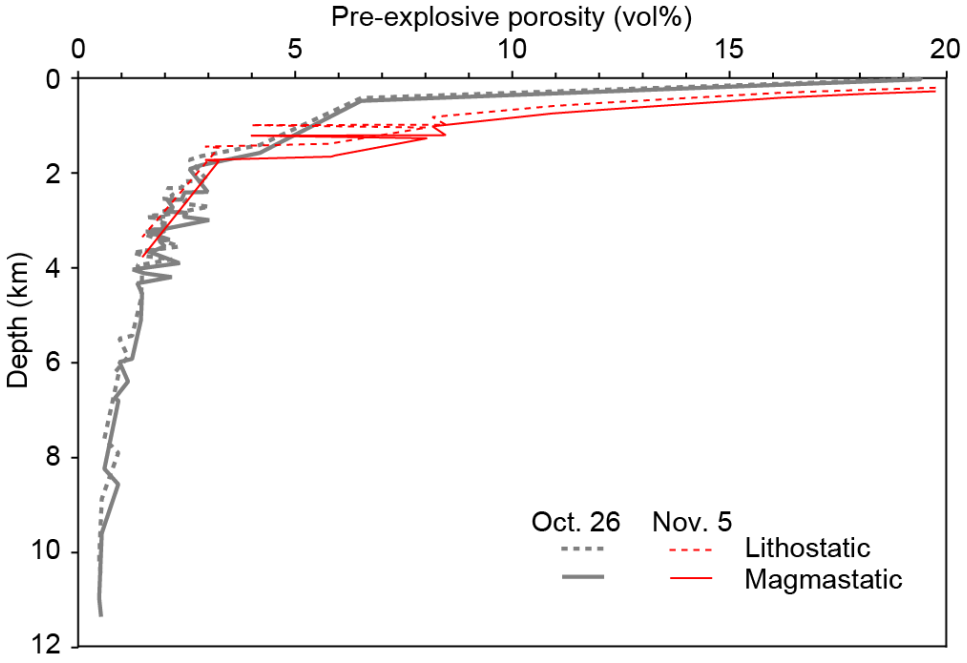


**Figure S5.** Pre-explosive porosities as a function of depth for the two events and for two overpressure scenarios (magmastatic and lithostatic). This information helped to sketch an approximate depth axis on Fig. 2.

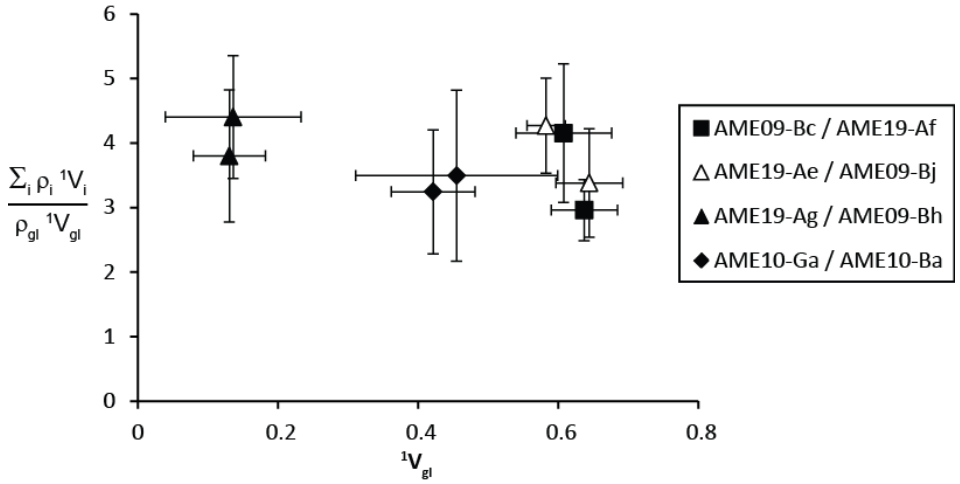


**Figure S6.** Glass volume fraction as a function of the inverse of glass weight fraction for sample pairs belonging to four different textural groups.

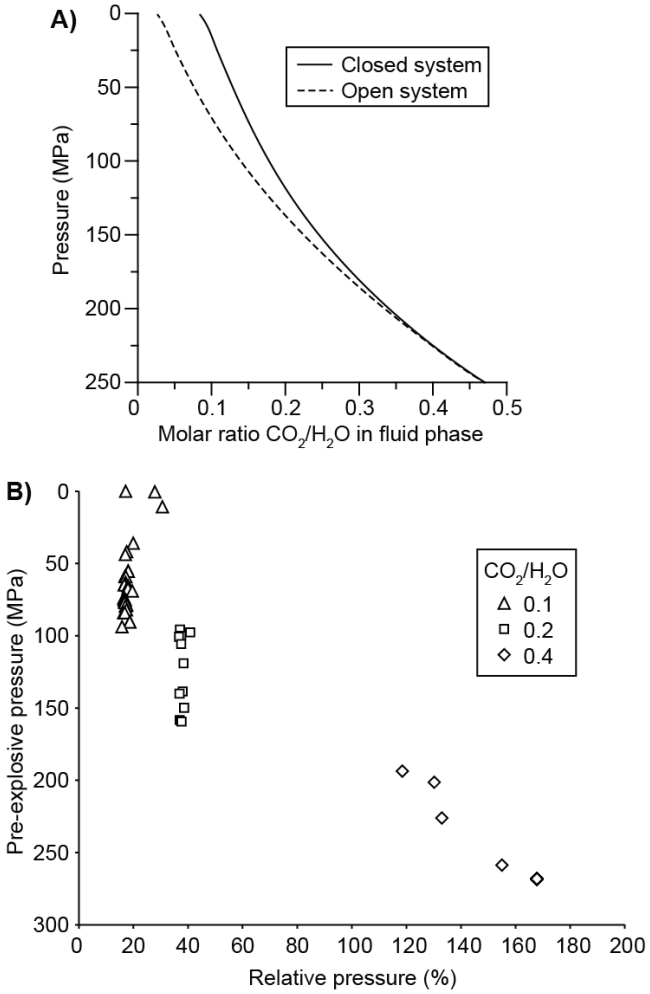


**Figure S7.** Evaluation of the effect of $CO_2$ on pre-explosive pressures. **A)** D-Compress runs simulating the evolution of $CO_2/H_2O$ in the fluid phase during decompression. **B)** Relative changes in pre-explosive pressures for the October 26 event compared to the pure $H_2O$ model outputs of Fig. 2 when three $CO_2/H_2O$ values are assumed (0.1, 0.2, and 0.4).

| Sample | $\delta^{18}O$ (‰) |
|---|---|
| October 26 | |
| AME10A-a | 6.099 (0.018) |
| AME10B-a | 6.402 (0.014) |
| AME10C-a | 6.201 (0.017) |
| AME10D-a | 6.202 (0.013) |
| AME10E-a | 6.104 (0.020) |
| AME10F-a | 4.970 (0.036) |
| AME10F-b | 5.648 (0.017) |
| AME10F-b | 5.912 (0.018) |
| AME10G-a | 5.630 (0.031) |
| AME10G-b | 6.141 (0.018) |
| November 5 | |
| AME19A-a | 6.167 (0.018) |
| AME19A-b | 5.220 (0.012) |

**Table S1.** Oxygen isotope composition of 2010 Merapi whole rock samples. Values are relative to the Standard Mean Ocean Water with one standard deviation in parenthesis. These data are reported graphically in Fig. 1.

| Sample | Vesicularity (vol%) | Phenocryst (vol%)[a] | Microlite (vol%) | Glass (vol%) | Bulk $H_2O$ (wt%) | Glass $H_2O$ (wt%) | Syn isol (%) | Syn conn (%) | Pre conn (%) |
|---|---|---|---|---|---|---|---|---|---|
| October 26 | | | | | | | | | |
| AME10-A1[b] | 38.7 (2.8) | 20.0 (0) | 23 (4) | 19 (2) | 1.06 (0.02) | 2.9 (0.6) | 3.1 | 63.4 | 33.5 |
| AME10-A2[b] | 34.7 (2.8) | 28.7 (0) | 23 (3) | 14 (3) | 1.12 (0.01) | 3.5 (0.8) | 1 | 67.3 | 31.8 |
| AME10-A3 | 47.2 (1.5) | 21.1 (0) | 22 (5) | 9 (6) | 1.00 (0.02) | 4.4 (3.0) | 3.8 | 66.7 | 29.5 |
| AME10-A4 | 41.1 (3.4) | 26.7 (0) | 20 (2) | 12 (2) | 1.00 (0.02) | 3.4 (0.5) | 1.0 | 69.5 | 29.5 |
| AME10-A5 | 37.2 (1.8) | 29.5 (0) | 18 (3) | 15 (3) | 0.99 (0.10) | 2.8 (0.7) | 4.9 | 59.9 | 35.3 |
| AME10-A6 | 36.9 (1.1) | 29.1 (0) | 16 (2) | 18 (2) | 1.00 (0.02) | 2.4 (0.3) | 5.7 | 59.0 | 35.3 |
| AME10-B1[b] | 32.5 (3.1) | 27.5 (0) | 26 (4) | 14 (2) | 1.25 (0.02) | 4.7 (1.0) | 3.5 | 66.4 | 30.1 |
| AME10-B2[b] | 35.5 (1.8) | 32.4 (0) | 14 (3) | 18 (1) | 1.12 (0.02) | 2.6 (0.3) | 3.8 | 67.1 | 29.1 |
| AME10-B4 | 36.4 (2.4) | 23.1 (0) | 32 (2) | 8 (2) | 1.08 (0.10) | 6.6 (1.9) | 2.8 | 65.9 | 31.3 |
| AME10-B5 | 28.4 (3.5) | 31.4 (0) | 31 (5) | 10 (3) | 1.16 (0.03) | 6.5 (2.9) | 1.7 | 75.6 | 22.7 |
| AME10-C1[b] | 38.9 (0.4) | 23.1 (0) | 26 (7) | 12 (3) | 1.15 (0.01) | 4.7 (1.2) | 1.9 | 68.3 | 29.8 |
| AME10-C2[b] | 32.7 (1.6) | 25.3 (0) | 29 (3) | 13 (2) | 1.06 (0.01) | 4.3 (0.6) | 0.7 | 79 | 20.3 |
| AME10-C3 | 34.7 (1.2) | 29.9 (0) | 16 (4) | 20 (2) | 1.03 (0.10) | 2.4 (0.5) | 3.7 | 63.8 | 32.5 |
| AME10-C4 | 34.7 (2.4) | 28.7 (0) | 21 (2) | 15 (3) | 1.01 (0.01) | 2.9 (0.6) | 4.5 | 73.6 | 21.9 |
| AME10-D1[b] | 42.0 (1.7) | 25.3 (0) | 21 (4) | 12 (1) | 1.02 (0.10) | 3.5 (0.6) | 1.4 | 76.4 | 22.1 |
| AME10-D2[b] | 31.7 (3.5) | 28.8 (0) | 25 (4) | 14 (2) | 0.96 (0.10) | 3.1 (1.0) | 2.0 | 71.9 | 26.1 |
| AME10-D3 | 31.6 (6.2) | 23.5 (0) | 24 (11) | 21 (7) | 1.06 (0.01) | 2.6 (1.1) | 3.8 | 68.1 | 28.1 |
| AME10-D4 | 30.0 (3.6) | 29.5 (0) | 20 (3) | 20 (3) | 1.11 (0.01) | 2.6 (0.4) | 2.5 | 56.8 | 40.7 |
| AME10-E1[b] | 26.5 (1.5) | 31.0 (0) | 23 (5) | 19 (3) | 1.04 (0.01) | 2.9 (0.6) | 0.6 | 77.9 | 21.5 |
| AME10-E2[b] | 51.1 (1.9) | 27.9 (0) | 15 (1) | 6 (1) | 1.06 (0.03) | 5.4 (1.3) | 4.7 | 69.2 | 26.0 |
| AME10-E3 | 27.1 (2.5) | 31.1 (0) | 23 (3) | 19 (1) | 0.89 (0.10) | 2.5 (0.3) | 2.5 | 70.1 | 27.3 |
| AME10-E4 | 36.8 (3.7) | 28.5 (0) | 17 (1) | 18 (3) | 1.19 (0.10) | 2.9 (0.4) | 2.5 | 67.6 | 30.0 |
| AME10-E5 | 27.4 (3.3) | 32.5 (0) | 30 (5) | 10 (1) | 1.17 (0.02) | 5.9 (1.5) | 1.9 | 71.1 | 27.0 |
| AME10-F1 | 10.7 (2.5) | 19.1 (0) | 29 (1) | 41 (2) | 0.49 (0.10) | 0.9 (0.2) | 1.6 | 88.7 | 9.7 |
| AME10-GA[b] | 24.6 (2.4) | 36.2 (0) | 25 (3) | 15 (2) | 0.96 (0.10) | 3.3 (0.6) | 2.9 | 71.4 | 25.7 |
| AME10-GB[b] | 24.0 (2.0) | 35.3 (0) | 32 (3) | 9 (2) | 0.92 (0.10) | 5.4 (1.6) | 0.4 | 83.5 | 16.1 |

| Sample | Vesicularity (vol%) | Phenocryst (vol%)[a] | Microlite (vol%) | Glass (vol%) | Bulk $H_2O$ (wt%) | Glass $H_2O$ (wt%) | Syn isol (%) | Syn conn (%) | Pre conn (%) |
|---|---|---|---|---|---|---|---|---|---|
| AME10-G1 | 26.5 (1.3) | 37.8 (0) | 17 (3) | 18 (3) | 0.81 (0.10) | 2.0 (0.5) | 2.7 | 69.0 | 28.3 |
| AME10-G2 | 23.9 (1.4) | 39.0 (0) | 23 (6) | 14 (5) | 0.85 (0.10) | 2.9 (1.6) | n.a. | n.a. | n.a. |
| AME10-G3 | 22.0 (1.9) | 32.3 (0) | 22 (6) | 23 (5) | 0.78 (0.02) | 2.1 (0.7) | 2.3 | 71.7 | 26 |
| AME10-Aa | 45.7 (2.5) | 24.0 (3.2) | 14 (4) | 37 (4) | 0.95 (0.06) | 2.6 (0.5) | 0.8 | 16.2 | 82.9 |
| AME10-Ac [c] | 45.7 (2.5) | 24.0 (3.2) | 14 (4) | 37 (4) | 0.93 (0.06) | 2.6 (0.5) | 0.8 | 16.2 | 82.9 |
| AME10-Ab | 38.5 (9.1) | 34.2 (8.4) | 10 (1) | 32 (2) | 0.85 (0.05) | 2.8 (0.6) | 1.9 | 11.2 | 86.9 |
| AME10-Db [c] | 38.5 (9.1) | 34.2 (8.4) | 10 (1) | 32 (2) | 1.00 (0.06) | 3.3 (0.7) | 1.9 | 11.2 | 86.9 |
| AME10-Bc | 40.3 (5.5) | 28.7 (6.5) | 13 (9) | 35 (8) | 0.97 (0.06) | 2.8 (0.8) | 0.8 | 15.9 | 83.3 |
| AME10-Bb [c] | 40.3 (5.5) | 28.7 (6.5) | 13 (9) | 35 (8) | 1.00 (0.06) | 3.0 (0.8) | 0.8 | 15.9 | 83.3 |
| AME10-Ca [c] | 40.3 (5.5) | 28.7 (6.5) | 13 (9) | 35 (8) | 1.04 (0.07) | 3.1 (0.9) | 0.8 | 15.9 | 83.3 |
| AME10-Cb | 46 (10) | 22.3 (6.0) | 11 (2) | 37 (9) | 0.81 (0.05) | 2.3 (0.7) | 2.5 | 33.5 | 64 |
| AME10-Da [c] | 46 (10) | 22.3 (6.0) | 11 (2) | 37 (9) | 1.02 (0.06) | 2.9 (0.8) | 2.5 | 33.5 | 64 |
| AME10-Ea | 57.2 (6.7) | 23.4 (6.2) | 8 (5) | 29 (6) | 0.89 (0.06) | 3.3 (0.9) | 0.5 | 39.0 | 60.5 |
| AME10-Eb [c] | 57.2 (6.7) | 23.4 (6.2) | 8 (5) | 29 (6) | 0.72 (0.05) | 2.6 (0.7) | 0.5 | 39.0 | 60.5 |
| AME10-Ec [c] | 57.2 (6.7) | 23.4 (6.2) | 8 (5) | 29 (6) | 0.85 (0.05) | 3.1 (0.9) | 0.5 | 39.0 | 60.5 |
| AME10-Ed [c] | 57.2 (6.7) | 23.4 (6.2) | 8 (5) | 29 (6) | 0.85 (0.05) | 3.1 (0.9) | 0.5 | 39.0 | 60.5 |
| AME10-Dc | 47.7 (8.5) | 32.0 (9.8) | 10 (3) | 26 (5) | 1.03 (0.07) | 4.2 (1.1) | 0.4 | 24.1 | 75.5 |
| AME10-Dd [c] | 47.7 (8.5) | 32.0 (9.8) | 10 (3) | 26 (5) | 0.93 (0.06) | 3.8 (1.0) | 0.4 | 24.1 | 75.5 |
| AME10-Fa | 29.5 (6.9) | 34.8 (4.6) | 16 (4) | 31 (4) | 0.13 (0.01) | 0.1 (0.1) | 0.8 | 35.7 | 63.5 |
| AME10-Fb [c] | 29.5 (6.9) | 34.8 (4.6) | 16 (4) | 31 (4) | 0.15 (0.01) | 0.2 (0.1) | 0.8 | 35.7 | 63.5 |
| AME10-Ga | 45 (14) | 25.3 (8.2) | 14 (13) | 32 (11) | 0.91 (0.06) | 3.0 (1.2) | 0.7 | 28.4 | 70.9 |
| AME10-Ba | 42.1 (6.0) | 31.6 (3.7) | 10 (4) | 34 (9) | 0.63 (0.04) | 1.7 (0.6) | 0.3 | 25.4 | 74.3 |
| November 5 | | | | | | | | | |
| AME19 A2 | 29.8 (3.1) | 31.2 (0.0) | 23 (3) | 16 (5) | 0.94 (0.10) | 3.1 (1.0) | 0.7 | 65.9 | 33.4 |
| AME19 A3 | 28.3 (3.2) | 27.5 (0.0) | 14 (3) | 30 (3) | 0.99 (0.10) | 1.9 (0.2) | 2.3 | 66.4 | 31.3 |
| AME19 A4 | 15.7 (1.4) | 29.3 (0.0) | 20 (2) | 35 (3) | 0.80 (0.10) | 1.5 (0.3) | 0.4 | 86.5 | 13.2 |
| AME19 A5 | 19.7 (4.2) | 29.7 (0.0) | 21 (4) | 29 (3) | 0.86 (0.10) | 1.9 (0.4) | 2.5 | 78.7 | 18.9 |

| Sample | Vesicularity (vol%) | Phenocryst (vol%)[a] | Microlite (vol%) | Glass (vol%) | Bulk $H_2O$ (wt%) | Glass $H_2O$ (wt%) | Syn isol (%) | Syn conn (%) | Pre conn (%) |
|---|---|---|---|---|---|---|---|---|---|
| MER13-01-1 [d] | 36.1 (2.5) | 30.5 (0.0) | 5.6 (0.6) | 28 (2) | 0.33 (0.05) | 0.5 (0.1) | 1.6 | 77.0 | 21.4 |
| MER13-01-3 [d] | 43.6 (1.4) | 31.8 (0.0) | 5.8 (1.3) | 19 (2) | 0.34 (0.07) | 0.6 (0.1) | 1.0 | 69.6 | 29.4 |
| MER13-01-6 [d] | 39.8 (3.6) | 19.6 (0.0) | 6.3 (1.5) | 34 (5) | 0.40 (0.01) | 0.6 (0.04) | 2.7 | 65.1 | 32.3 |
| AME19-Ad | 60.8 (6.8) | 24.5 (6.7) | 3.9 (1.3) | 26 (5) | 0.33 (0.04) | 1.3 (0.4) | 0.4 | 51.1 | 48.6 |
| AME19-Af [c] | 60.8 (6.8) | 24.5 (6.7) | 3.9 (1.3) | 26 (5) | 0.32 (0.02) | 1.3 (0.3) | 0.4 | 51.1 | 48.6 |
| AME19-Ac | 58.2 (2.7) | 25.8 (3.6) | 5.0 (1.5) | 26 (3) | 0.42 (0.05) | 1.6 (0.4) | 0.2 | 38.2 | 61.6 |
| AME19-Ae [c] | 58.2 (2.7) | 25.8 (3.6) | 5.0 (1.5) | 26 (3) | 0.43 (0.05) | 1.6 (0.4) | 0.2 | 38.2 | 61.6 |
| AME19-Aa | 51.7 (5.1) | 28.2 (6.5) | 6.0 (5.3) | 30 (6) | 0.39 (0.04) | 1.2 (0.4) | 0.3 | 25.6 | 74.0 |
| AME19-Ab [c] | 51.7 (5.1) | 28.2 (6.5) | 6.0 (5.3) | 30 (6) | 0.32 (0.04) | 0.9 (0.3) | 0.3 | 25.6 | 74.0 |
| AME19-Ag [c] | 51.7 (5.1) | 28.2 (6.5) | 6.0 (5.3) | 30 (6) | 0.30 (0.02) | 0.9 (0.3) | 0.3 | 25.6 | 74.0 |

[a] A standard deviation of 0.0 means that only one large-scale (×50) SEM image was analyzed for that sample.
[b] Sample pairs issued from the same clast AME10-X.
[c] Proportions of vesicles, phenocrysts, microlite, and glass are identical to the sample immediately above because they belong to the same textural group (e.g., AME10-Bb and AME10-Ca are in the same group as AME10-Bc).
[d] The standard PYRO was used instead of SOIL.

**Table S2**. Results from the textural and glass water analyses. Values in parenthesis are one standard deviation. Columns "Syn isol", "Syn conn", and "Pre conn" respectively represent the proportions (to 100%) of syn-explosive and isolated vesicles, syn-explosive and connected vesicles, and pre-explosive and connected vesicles. Not analyzed is "n.a.".

| Sample | μphenocryst (vol%) | Oxides (vol%) |
|---|---|---|
| October 26 | | |
| AME10-A1 | 5.1 | 1.5 (0.3) |
| AME10-A2 | 5.2 | 1.6 (0.2) |
| AME10-A3 | 5.0 | 3.3 (1.3) |
| AME10-A4 | 5.4 | 1.9 (0.8) |
| AME10-A5 | 6.7 | 2.3 (0.3) |
| AME10-A6 | 5.7 | 3.5 (0.7) |
| AME10-B1 | 4.8 | 7.0 (2.8) |
| AME10-B2 | 5.1 | 2.0 (0.7) |
| AME10-B4 | 5.9 | 2.1 (0.5) |
| AME10-B5 | 4.4 | 4.7 (2.6) |
| AME10-C1 | 5.2 | 6.7 (2.8) |
| AME10-C2 | 4.8 | 3.4 (1.7) |
| AME10-C3 | 6.1 | 3.1 (0.5) |
| AME10-C4 | 5.1 | 2.1 (0.7) |
| AME10-D1 | 4.6 | 4.4 (1.5) |
| AME10-D2 | 3.5 | 3.5 (2.1) |
| AME10-D3 | 4.5 | 2.4 (0.5) |
| AME10-D4 | 4.4 | 2.5 (0.8) |
| AME10-E1 | 5.1 | 4.0 (1.7) |
| AME10-E2 | 5.1 | 1.9 (1.2) |
| AME10-E3 | 5.8 | 4.0 (1.3) |
| AME10-E4 | 5.4 | 2.1 (0.4) |
| AME10-E5 | 4.0 | 3.9 (3.4) |
| AME10-F1 | 1.2 | 4.5 (1.1) |
| AME10-GA | 4.8 | 6.5 (1.9) |
| AME10-GB | 4.5 | 5.8 (1.2) |
| AME10-G1 | 6.9 | 1.6 (0.2) |
| AME10-G2 | 6.0 | 2.9 (0.2) |
| AME10-G3 | 8.4 | 4.7 (1.3) |
| November 5 | | |
| AME19-A2 | 5.8 | 6.2 (3.2) |
| AME19-A3 | 6.8 | 3.5 (1.3) |
| AME19-A4 | 5.4 | 4.7 (3.8) |
| AME19-A5 | 7.0 | 2.2 (0.3) |
| MER13-01-1 | 3.8 | 3.4 (1.2) |
| MER13-01-3 | 8.5 | 2.6 (0.7) |
| MER13-01-6 | 3.0 | 3.5 (1.4) |

**Table S3**. Results specific to the SEM textural analysis. Values in parenthesis are one standard deviation.

| Sample | Oxide (vol%) | Opx (vol%) | Cpx+Amph (vol%) | Plag (vol%) | Ca (vol%) | Glass (vol%) |
|---|---|---|---|---|---|---|
| October 26 | | | | | | |
| AME10-Aa | 2.9 (0.5) | 1.6 (0.8) | 10.2 (4.5) | 46 (8) | 1.3 (0.8) | 37.5 (4.5) |
| AME10-Ac | 2.9 (0.5) | 1.6 (0.8) | 10.2 (4.5) | 46 (8) | 1.3 (0.8) | 37.5 (4.5) |
| AME10-Ab | 2.4 (1.0) | 1.1 (0.1) | 6.0 (2.9) | 58 (17) | 0.8 (0.1) | 31.8 (1.6) |
| AME10-Db | 2.4 (1.0) | 1.1 (0.1) | 6.0 (2.9) | 58 (17) | 0.8 (0.1) | 31.8 (1.6) |
| AME10-Bc | 3.9 (1.0) | 1.8 (0.5) | 14 (13) | 51 (7) | 0.5 (0.4) | 34.7 (8.1) |
| AME10-Bb | 3.9 (1.0) | 1.8 (0.5) | 14 (13) | 51 (7) | 0.5 (0.4) | 34.7 (8.1) |
| AME10-Ca | 3.9 (1.0) | 1.8 (0.5) | 14 (13) | 51 (7) | 0.5 (0.4) | 34.7 (8.1) |
| AME10-Cb | 2.4 (1.0) | 3.0 (1.4) | 3.5 (1.0) | 52 (12) | 1.0 (0.4) | 37.4 (8.8) |
| AME10-Da | 2.4 (1.0) | 3.0 (1.4) | 3.5 (1.0) | 52 (12) | 1.0 (0.4) | 37.4 (8.8) |
| AME10-Ea | 3.6 (1.2) | 1.6 (0.7) | 8.8 (5.0) | 55 (13) | 1.4 (0.7) | 28.9 (6.0) |
| AME10-Eb | 3.6 (1.2) | 1.6 (0.7) | 8.8 (5.0) | 55 (13) | 1.4 (0.7) | 28.9 (6.0) |
| AME10-Ec | 3.6 (1.2) | 1.6 (0.7) | 8.8 (5.0) | 55 (13) | 1.4 (0.7) | 28.9 (6.0) |
| AME10-Ed | 3.6 (1.2) | 1.6 (0.7) | 8.8 (5.0) | 55 (13) | 1.4 (0.7) | 28.9 (6.0) |
| AME10-Dc | 4.4 (5.0) | 1.1 (0.4) | 6.4 (3.3) | 60 (12) | 0.9 (0.5) | 26.4 (5.1) |
| AME10-Dd | 4.4 (5.0) | 1.1 (0.4) | 6.4 (3.3) | 60 (12) | 0.9 (0.5) | 26.4 (5.1) |
| AME10-Fa | 4.1 (2.1) | 4.3 (2.4) | 16.7 (3.3) | 42 (6) | 1.2 (0.3) | 31.1 (3.8) |
| AME10-Fb | 4.1 (2.1) | 4.3 (2.4) | 16.7 (3.3) | 42 (6) | 1.2 (0.3) | 31.1 (3.8) |
| AME10-Ga | 4.4 (4.4) | 3.0 (0.9) | 8.3 (6.6) | 51 (12) | 1.0 (0.4) | 32 (11) |
| AME10-Ba | 3.4 (1.8) | 1.9 (1.4) | 14.8 (7.6) | 49 (12) | 1.6 (0.4) | 34.5 (8.6) |
| November 5 | | | | | | |
| AME19-Ad | 1.5 (0.3) | 1.3 (1.0) | 2.7 (1.1) | 67 (15) | 0.8 (0.6) | 26.2 (5.4) |
| AME19-Af | 1.5 (0.3) | 1.3 (1.0) | 2.7 (1.1) | 67 (15) | 0.8 (0.6) | 26.2 (5.4) |
| AME19-Ac | 1.6 (0.3) | 1.2 (1.0) | 7.3 (3.6) | 63 (11) | 0.3 (0.2) | 25.8 (3.2) |
| AME19-Ae | 1.6 (0.3) | 1.2 (1.0) | 7.3 (3.6) | 63 (11) | 0.3 (0.2) | 25.8 (3.2) |
| AME19-Aa | 4.4 (2.0) | 1.0 (0.4) | 12.1 (4.4) | 52 (14) | 0.7 (0.3) | 29.9 (6.5) |
| AME19-Ab | 4.4 (2.0) | 1.0 (0.4) | 12.1 (4.4) | 52 (14) | 0.7 (0.3) | 29.9 (6.5) |
| AME19-Ag | 4.4 (2.0) | 1.0 (0.4) | 12.1 (4.4) | 52 (14) | 0.7 (0.3) | 29.9 (6.5) |

**Table S4**. Results specific to the EDS textural analysis. Values in parenthesis are one standard deviation.

| Sample | Melt $H_2O$ (wt%) | Pressure (MPa) | Porosity (vol%)[a] | Total gas (wt%) | Magm. depth (km) | Lith. depth (km) |
|---|---|---|---|---|---|---|
| October 26 | | | | | | |
| AME10-A1 | 3.1 (0.6) | 75 (+22,-25) | 1.94 (0.08) | 0.37 | 3.3 | 3.0 |
| AME10-A2 | 3.7 (0.9) | 101 (+34,-38) | 1.37 (0.06) | 0.35 | 4.3 | 3.9 |
| AME10-A3 | 4.7 (3.2) | 150 (+124,-174) | 1.15 (0.03) | 0.44 | 6.4 | 5.9 |
| AME10-A4 | 3.7 (0.6) | 100 (+22,-24) | 1.53 (0.09) | 0.39 | 4.3 | 3.9 |
| AME10-A5 | 3.1 (0.7) | 75 (+25,-29) | 1.92 (0.05) | 0.36 | 3.2 | 2.9 |
| AME10-A6 | 2.7 (0.4) | 59 (+13,-14) | 2.39 (0.04) | 0.36 | 2.6 | 2.3 |
| AME10-B1 | 4.9 (1.0) | 158 (+48,-53) | 0.84 (0.04) | 0.34 | 6.8 | 6.2 |
| AME10-B2 | 2.8 (0.3) | 63 (+11,-12) | 2.19 (0.06) | 0.35 | 2.7 | 2.5 |
| AME10-B4 | 6.9 (2.0) | 268 (+106,-118) | 0.53 (0.02) | 0.36 | 11.4 | 10.5 |
| AME10-B5 | 6.7 (3.0) | 259 (+153,-184) | 0.49 (0.03) | 0.32 | 11.0 | 10.1 |
| AME10-C1 | 4.9 (1.2) | 159 (+57,-64) | 0.93 (0.01) | 0.37 | 6.8 | 6.3 |
| AME10-C2 | 4.5 (0.7) | 140 (+30,-33) | 0.95 (0.02) | 0.34 | 6.0 | 5.5 |
| AME10-C3 | 2.6 (0.6) | 56 (+18,-20) | 2.45 (0.04) | 0.35 | 2.4 | 2.2 |
| AME10-C4 | 3.1 (0.7) | 76 (+24,-27) | 1.81 (0.06) | 0.35 | 3.3 | 3.0 |
| AME10-D1 | 3.8 (0.6) | 106 (+25,-27) | 1.47 (0.04) | 0.40 | 4.5 | 4.1 |
| AME10-D2 | 3.3 (1.0) | 84 (+37,-43) | 1.55 (0.08) | 0.33 | 3.6 | 3.3 |
| AME10-D3 | 2.8 (1.2) | 64 (+37,-47) | 2.02 (0.18) | 0.33 | 2.8 | 2.5 |
| AME10-D4 | 2.8 (0.4) | 65 (+14,-15) | 1.96 (0.09) | 0.32 | 2.8 | 2.5 |
| AME10-E1 | 3.1 (0.7) | 74 (+23,-26) | 1.64 (0.03) | 0.31 | 3.2 | 2.9 |
| AME10-E2 | 5.7 (1.4) | 202 (+67,-74) | 0.93 (0.03) | 0.47 | 8.6 | 7.9 |
| AME10-E3 | 2.7 (0.3) | 59 (+11,-12) | 2.06 (0.07) | 0.31 | 2.6 | 2.3 |
| AME10-E4 | 3.2 (0.4) | 77 (+15,-16) | 1.84 (0.10) | 0.36 | 3.3 | 3.0 |
| AME10-E5 | 6.1 (1.5) | 226 (+78,-87) | 0.55 (0.03) | 0.31 | 9.6 | 8.9 |
| AME10-F1 | 1.0 (0.2) | 11 (+4,-5) | 6.51 (1.54) | 0.19 | 0.5 | 0.4 |
| AME10-GA | 3.5 (0.6) | 94 (+25,-28) | 1.26 (0.04) | 0.30 | 4.0 | 3.7 |
| AME10-GB | 5.6 (1.6) | 194 (+80,-91) | 0.61 (0.02) | 0.30 | 8.2 | 7.6 |
| AME10-G1 | 2.2 (0.6) | 42 (+16,-18) | 2.85 (0.04) | 0.31 | 1.8 | 1.6 |
| AME10-G2 | 3.1 (1.7) | 75 (+54,-75) | 1.56 (0.03) | 0.30 | 3.2 | 2.9 |
| AME10-G3 | 2.3 (0.8) | 44 (+21,-25) | 2.57 (0.06) | 0.29 | 1.9 | 1.7 |
| AME10-Aa | 2.9 (0.5) | 68 (+18,-19) | 2.43 (0.10) | 0.42 | 2.9 | 2.7 |
| AME10-Ac | 2.9 (0.5) | 66 (+17,-19) | 2.50 (0.10) | 0.42 | 3.2 | 2.9 |
| AME10-Ab | 3.1 (0.6) | 74 (+21,-23) | 1.96 (0.29) | 0.37 | 2.8 | 2.6 |
| AME10-Db | 3.6 (0.7) | 96 (+27,-30) | 1.52 (0.23) | 0.37 | 4.1 | 3.7 |
| AME10-Bc | 3.1 (0.9) | 75 (+30,-35) | 2.00 (0.17) | 0.38 | 3.2 | 2.9 |
| AME10-Bb | 3.2 (0.9) | 80 (+32,-37) | 1.88 (0.16) | 0.38 | 3.4 | 3.1 |
| AME10-Ca | 3.3 (0.9) | 84 (+34,-39) | 1.78 (0.16) | 0.38 | 3.6 | 3.3 |
| AME10-Cb | 2.6 (0.7) | 55 (+22,-26) | 2.98 (0.54) | 0.43 | 2.4 | 2.2 |
| AME10-Da | 3.2 (0.9) | 79 (+32,-37) | 2.11 (0.41) | 0.43 | 3.4 | 3.1 |
| AME10-Ea | 3.6 (1.0) | 98 (+37,-42) | 2.16 (0.32) | 0.54 | 4.2 | 3.8 |
| AME10-Eb | 3.0 (0.8) | 69 (+26,-30) | 3.02 (0.42) | 0.54 | 3.0 | 2.7 |

| Sample | Melt $H_2O$ (wt%) | Pressure (MPa) | Porosity (vol%)[a] | Total gas (wt%) | Magm. depth (km) | Lith. depth (km) |
|---|---|---|---|---|---|---|
| AME10-Ec | 3.5 (1.0) | 91 (+34,-39) | 2.32 (0.34) | 0.54 | 3.9 | 3.6 |
| AME10-Ed | 3.5 (1.0) | 90 (+34,-39) | 2.32 (0.34) | 0.54 | 3.9 | 3.5 |
| AME10-Dc | 4.5 (1.2) | 139 (+51,-58) | 1.25 (0.21) | 0.44 | 5.9 | 5.4 |
| AME10-Dd | 4.1 (1.1) | 119 (+44,-50) | 1.45 (0.24) | 0.44 | 5.1 | 4.7 |
| AME10-Fa | 0.1 (0.1) | 0.1 (+0.1,-0.4) | 19.4 (5.4) | 0.01 | 0.006 | 0.005 |
| AME10-Fb | 0.2 (0.1) | 0.6 (+0.4,-0.9) | 19.4 (5.4) | 0.03 | 0.03 | 0.02 |
| AME10-Ga | 3.3 (1.3) | 82 (+44,-54) | 2.00 (0.58) | 0.42 | 3.5 | 3.2 |
| AME10-Ba | 2.0 (0.7) | 36 (+16,-20) | 4.19 (0.35) | 0.39 | 1.6 | 1.4 |
| November 5 | | | | | | |
| AME19-A2 | 3.4 (1.0) | 86 (+37,-44) | 1.49 (0.06) | 0.32 | 3.8 | 3.4 |
| AME19-A3 | 2.1 (0.3) | 38 (+7,-8) | 3.24 (0.13) | 0.32 | 1.8 | 1.5 |
| AME19-A4 | 1.7 (0.4) | 26 (+8,-10) | 3.98 (0.06) | 0.27 | 1.2 | 1.0 |
| AME19-A5 | 2.1 (0.4) | 38 (+11,-12) | 2.93 (0.14) | 0.28 | 1.7 | 1.5 |
| MER13-01-1 | 0.7 (0.1) | 6 (+1,-1) | 19.75 (0.24) | 0.36 | 0.3 | 0.2 |
| MER13-01-3 | 0.9 (0.2) | 9 (+2,-3) | 16.19 (0.15) | 0.41 | 0.4 | 0.3 |
| MER13-01-6 | 0.8 (0.1) | 7 (+1,-1) | 18.08 (0.36) | 0.38 | 0.4 | 0.3 |
| AME19-Ad | 1.7 (0.5) | 27 (+10,-11) | 8.04 (0.82) | 0.59 | 1.3 | 1.1 |
| AME19-Af | 1.7 (0.5) | 26 (+9,-10) | 8.46 (0.83) | 0.59 | 1.2 | 1.0 |
| AME19-Ac | 2.0 (0.5) | 35 (+11,-12) | 5.92 (0.26) | 0.55 | 1.7 | 1.4 |
| AME19-Ae | 2.0 (0.5) | 36 (+11,-12) | 5.83 (0.26) | 0.55 | 1.7 | 1.4 |
| AME19-Aa | 1.5 (0.5) | 22 (+9,-11) | 8.16 (0.52) | 0.48 | 1.0 | 0.8 |
| AME19-Ab | 1.3 (0.4) | 16 (+7,-8) | 10.92 (0.58) | 0.48 | 0.8 | 0.6 |
| AME19-Ag | 1.2 (0.4) | 14 (+6,-7) | 12.12 (0.58) | 0.48 | 0.7 | 0.5 |

[a] Only positive errors are reported since negative and positive errors differ by <14%.

**Table S5**. Results on the pre-explosive conduit conditions. Values in parenthesis are one standard deviation and the plus and minus signs indicate positive and negative errors. Total gas is the total amount of syn-explosive gas. Depths are measured from the vent down and are considering respectively magma-static (Magm. depth) and litho-static (Lith. depth) conduit pressure gradient. These data are reported graphically in Figs. 2-3.